Int. J. Electrochem. Sci., 9 **(2014)** 1207 - 1220

International Journal of
ELECTROCHEMICAL
SCIENCE
www.electrochemsci.org

Fast and Facile Synthesis of $LiMn_2O_4$ Nanorods for Li Ion Battery by Microwave Assisted Hydrothermal and Solid State Reaction Methods

B. Nageswara Rao[1], P. Muralidharan[2], P. Ramesh Kumar[1], M. Venkateswarlu[3,], N. Satyanarayana[1,*]*

[1] Department of Physics, Pondicherry University, Pondicherry 605014, India
[2] Department of Chemistry, Rajiv Gandhi College of Engineering & Technology, Pondicherry 607402, India
[3] R&D, Amara Raja Batteries Ltd., Karakambadi, Tirupathi-517520, India
[*]E-mails: nallanis2011@gmail.com(N.Satyanarayana); mvu@amararaja.co.in (M.Venkateswarlu);

Received: 30 September 2013 / *Accepted:* 26 November 2013 / *Published:* 5 January 2014

A rapid and efficient two-steps growth strategy has been adopted to synthesize monodisperse single-crystalline spinel $LiMn_2O_4$ nanorods. The first step is to synthesize crystalline β-MnO_2 nanorods through rapid microwave hydrothermal process followed by second step as solid state reaction between β-MnO_2 nanorods and $LiOH.H_2O$ to obtain pure spinel $LiMn_2O_4$ nanorods. In addition, the possible formation mechanism of the β-MnO_2 and spinel $LiMn_2O_4$ nanorods was also discussed. The spinel $LiMn_2O_4$ nanorods have an average diameter of 190 nm and length of 0.8-1.3 μm. Galvanostatic battery testing shows that the spinel $LiMn_2O_4$ nanorods have delivered a stable charge and discharge capacities of 98 and 96 $mAhg^{-1}$, respectively, after 50 cycles at 0.1C rate in the voltage range 3.1-4.4 V. The cathode material exhibits good electrochemical performance even at high C-rates. The developed $LiMn_2O_4$ nanorods show a higher coulombic efficiency and also good rate capability attributed to the formation of the single-crystalline spinel $LiMn_2O_4$ with nanorod morphology.

Keywords: Lithium manganese oxide, Nanorods, Microwave hydrothermal reaction, Cycleability, Coulombic efficiency.

1. INTRODUCTION

Lithium ion battery technologies with high energy and power density have been widely investigated for portable electronic gadgets, power tools, electric vehicles (EVs) and hybrid electric vehicles (HEVs), etc., [1-4]. In general, lithium ion batteries can provide higher energy density ($Whkg^{-1}$) with limited power density (Wkg^{-1}) compared to double layer and pseudocapacitors. Hence, the development of better specific power density lithium ion batteries is of interest for EVs and HEVs. The

most commonly used cathode material in commercial Li-ion batteries is layer structured $LiCoO_2$ mainly due to its ease in production, high volumetric and gravimetric energy density, high rates performance, good cycle stability and higher operating potential [5,6]. However, the high cost, toxicity and limited abundance of cobalt have been limited its applications. Therefore, alternative cost effective cathode materials have been received great attention to replace $LiCoO_2$. Among the studied cathode materials, the spinel $LiMn_2O_4$, with a theoretical storage capacity of 148 $mAhg^{-1}$, has been recognized as the most potential candidate to replace $LiCoO_2$ in commercialized lithium ion batteries, because of its high abundance, cost effective and environmental benign [7-12]. Despite of several benefits of spinel cathode; the reversible capacity and cycleability of $LiMn_2O_4$ have to be improved further by controlling the manganese dissolution, John-Teller distortion and decomposition of electrolyte. The application of the $LiMn_2O_4$ as cathode in high power lithium-ion system requires faster kinetics of the electrodes, which can be achieved by means of nanostructured materials.

Nanostructured electrode materials exhibit higher surface area to volume ratio and allow for a larger surface area contact at the electrode-electrolyte interface. Among various morphological nanostructured electrode materials; one-dimensional (1D) nanorods, nanowires, and nanotubes have shown greatest advantages over bulk materials [13-15]. In addition to larger surface area to volume ratio, the particle size and its one-dimensional morphology provide an efficient electron transport pathways and facile strain relaxation during the cycling operation of a battery [13].

Several innovative and traditional processes have been used to develop spinel $LiMn_2O_4$ nanoparticles and nanorods and the most promising synthesis methods are: sol-gel, combustion, solution phase, and hydrothermal [16-20]. Recently, Zhan et al., have been developed single-crystalline $LiMn_2O_4$ nanorods using β-MnO_2 nanorods. The β-MnO_2 was synthesized by hydrothermal process. The capacity test results showed that the discharge capacity was found to be 125 $mAhg^{-1}$ at 0.5 C-rate [21]. W.Tang et al. studied spinel $LiMn_2O_4$ nanorods, synthesized by hydrothermal, in combination with traditional solid state reaction method, and the material exhibited good electrochemical performance even at higher C-rates [22]. However, these methods have some limitations such as longer reaction times (48 to 72 hours), non-uniform distribution of particles, low yield, etc. In conventional hydrothermal synthesis, the walls of the reactor are heated up by conduction and the core of the sample requires longer time to achieve the desired temperature inside the reactor which may leads to non-uniformity in temperature profile. Thus, several researchers have been focused on to develop a synthesis approach, which can yield higher product with uniform particle distribution at relatively shorter reaction time. Recently, microwave assisted hydrothermal/solvothermal synthesis approach has been extremely appealing as it can shorten the reaction time from several hours to several minutes with cleaner and high yield of the product and also enormous energy savings, which helps in commercialization of the product [23-25].

Thus, we are motivated to design and develop a facile growth strategy to synthesize β-MnO_2 nanorods via microwave assisted hydrothermal process followed by single-crystalline spinel $LiMn_2O_4$ nanorods growth through solid state reaction method. The prepared samples were characterized using X-ray diffractometer (XRD), scanning electron microscopy (SEM), field emission scanning electron microscopy (FE-SEM), transmission electron microscopy (TEM), fourier transform infra-red (FTIR) and Raman spectroscopy (RS) techniques. The electrochemical performance of the nanorods cathode

material has been evaluated by charge/discharge studies at different C-rates, at ambient temperature. The impedance of the electrochemical cell has been studied by electrochemical impedance spectroscopy (EIS) technique.

2. EXPERIMENTAL

2.1 Synthesis of β-MnO_2 Nanorods

All the commercial available grade respective precursor chemicals were used without further purification. The $Mn(CH_3COO)_2.4H_2O$ (Merck), $Na_2S_2O_8$ (Aldrich), and deionized water were used to prepare β-MnO_2 nanorods. In a typical reaction, 0.008:0.008 molar ratio of $Mn(CH_3COO)_2.4H_2O$ and $Na_2S_2O_8$ were dissolved in 70 ml of deionized water under continuous stirring at room temperature to form a clear homogenous solution. The transparent solution was transferred to a 100 ml teflon liner vessel, which has an outer high strength sleeve made up of advanced composite material. The vessel was sealed and placed on a rotating (180°) turn table for uniform heating in a microwave accelerated reaction system (MARS, CEM corporation, USA) at 120 °C for 15, 30 and 90 minutes for microwave hydrothermal reaction. After the reaction, the grown products were subsequently washed with deionized water followed by acetone washing to remove excess sulphate ions and remnants by high speed centrifugation. The obtained powder was dried at 120 °C for 12 h in an air circulated oven.

2.2 Synthesis of $LiMn_2O_4$ Nanorods

In order to prepare $LiMn_2O_4$ nanorods, 1:2 molar ratio of $LiOH.H_2O$ (Sigma Aldrich) and as prepared β-MnO_2 nanorods were dispersed in 5 ml of high purity ethanol to form a slurry, ground for several hours to form a fine mixture. The resultant mixture was dried out at room temperature. The process was repeated for three times to form a well-mixed powder and calcined at 700 ^oC for 10 h in air to grow $LiMn_2O_4$ nanorods. A schematic illustration of possible growth mechanisms of β-MnO_2 at different reaction time intervals and also formation of the $LiMn_2O_4$ nanorods are shown in Fig.1.

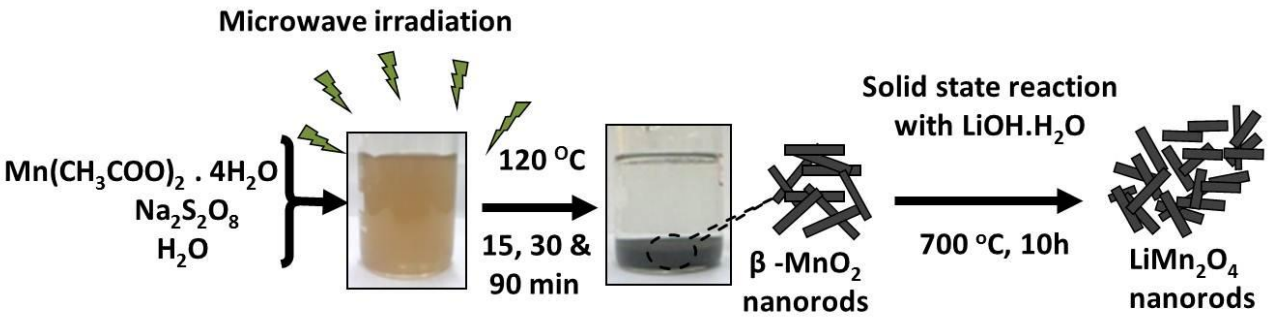

Figure 1. Schematic illustration of possible growth of β-MnO_2 nanorods and $LiMn_2O_4$ nanorods.

2.3 Characterization

The crystallinity and phase purity of the grown samples were identified by recording XRD patterns (X'pert PRO MPD, PANalytical) with Cu Kα radiation (λ=0.154 nm at 40 kV and 30 mA). The structure of the grown samples were identified using FTIR spectroscopy (Shimadzu FTIR-8000 spectrometer). Raman spectrum was recorded at room temperature on Renishaw in Via Raman Microscope (Ar-Ne Laser source, 514 nm line radiation). The size and morphology of the synthesized samples were examined by SEM (Hitachi, S-3400N), FE-SEM (SUPRA ^{TM} 55) and TEM (Philips, CM200 model).

2.4 Electrochemical measurement

The electrochemical measurements were made on swagelok-type cells. The electrode was prepared by mixing 70 wt. % of active material with 20 wt. % super P carbon black and 10 wt. % poly-vinylidene fluoride (PVDF) in N-methylpyrrolidone (NMP) solvent. The resultant slurry was coated on the Aluminum (Al) foil and dried out at 100 ^{o}C in an oven. The resultant cathode composite electrode was made into circular electrodes. The lithium foil was used as anode and a 1 M solution of $LiPF_6$ in ethylene carbonate (EC) and dimethyl carbonate (DMC) (EC: DMC = 1:1) was used as electrolyte [LP 30, Merck]. The cells were assembled in an Argon-filled dry glove box (Mbraun, MB10 compact) with electrodes and Whatman GF/D borosilicate glass-fibre separator. The cyclic voltammetry (CV) and in-situ electrochemical impedance spectroscopy (EIS) measurements of first cycle at different potentials were measured using Biologic Science Instruments (Model: VMP3) in the frequency range between 0.1 MHz to 10 mHz under AC stimuli with 5 mV of amplitude. The cells were galvanostatically studied using battery cycle tester (Arbin, model BT2000) in the voltage range 3.1V - 4.4 V, at ambient conditions.

3. RESULTS AND DISCUSSION

The SEM images of the β-MnO_2 samples obtained at different reaction times are shown in Fig.2 (a, c and e). The SEM images showed that the growth of the β-MnO_2 nanorods followed initial nuclei formation and continued to grow in unidirection into one–dimensional nanorods with respect to reaction time under uniform high pressure in the vessel. It can be seen that the β-MnO_2 samples obtained at 15 (Fig.2a) and 30 (Fig.2c) minutes reaction times have confirmed the initialization of nuclei process for the formation of nanorod morphology. Fig. 2e shows further increase of reaction time to 90 minutes leads to the formation of well grown nanorods with an average diameter of 90 nm and length of 1.2-1.8 μm. Further, the phase purity and crystal structure of as-prepared samples were examined by recording powder XRD patterns. Figs. 2 (b, d and f) show the XRD patterns of the β-MnO_2 samples obtained at 15, 30 and 90 minutes, respectively. The observed diffraction peaks were indexed to the tetragonal structure of β-MnO_2 (JCPDS card No. 07-3716) with *P42/mnm* space group.

As shown in Fig.2 (b, d and f), the crystalline nature of the β-MnO_2 increases with reaction time and highly crystalline β-MnO_2 phase was obtained at 90 minutes (Fig.2f).

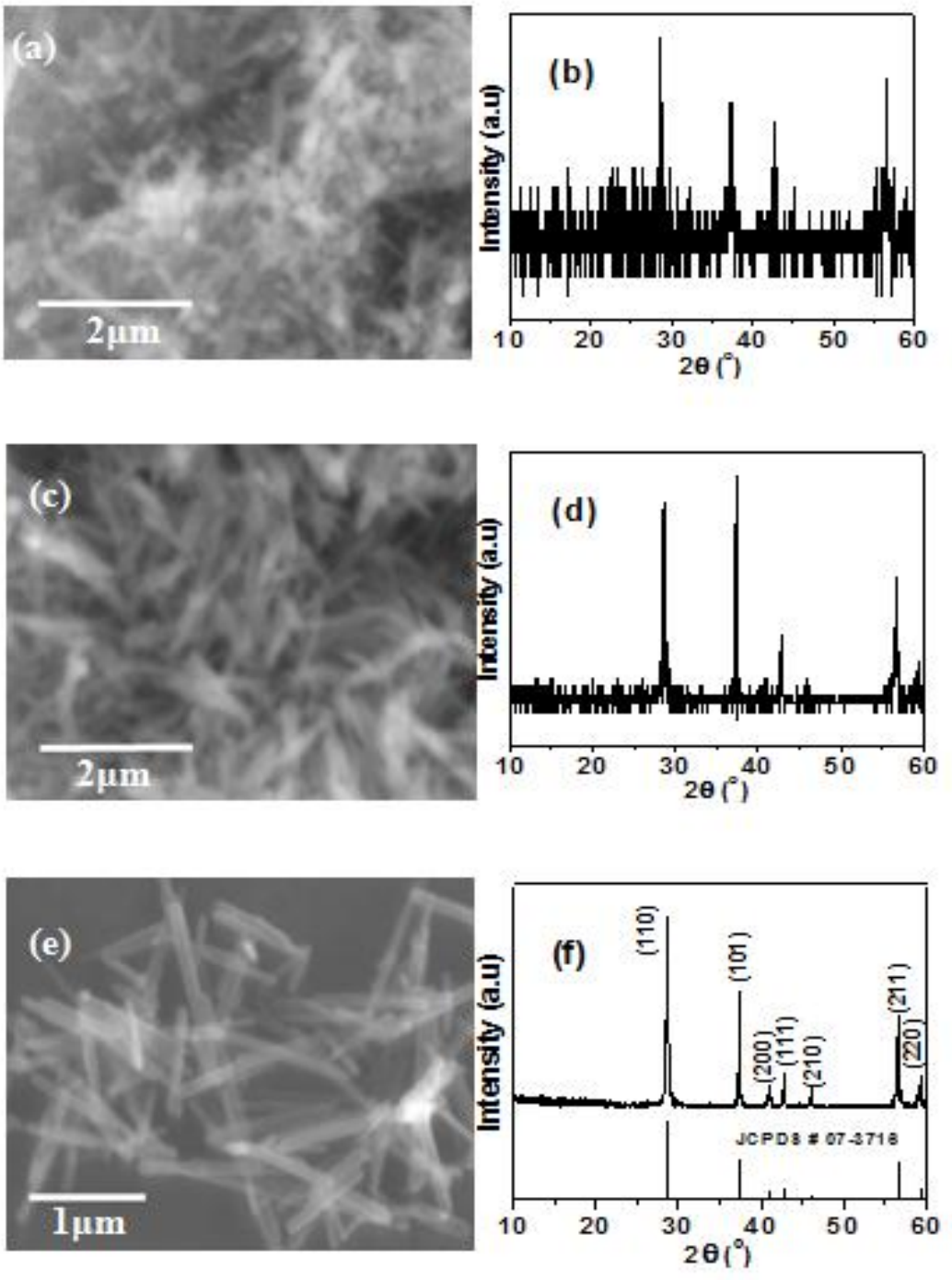

Figure 2. SEM images and XRD patterns of β-MnO_2 obtained at 120 ^{o}C for different reaction times,15 minutes (a, b), 30 minutes (c, d) and 90 minutes (e, f)).

Fig.3 (a, b and c) shows the FE-SEM images and XRD pattern of the $LiMn_2O_4$ nanorods obtained at 700 ^{o}C. As shown in Figs. 3(a & b), the FE-SEM images of the $LiMn_2O_4$ confirmed the

nanorod morphology with an average diameter of 190 nm and length of 0.8-1.3 μm. It is notable that the nanorod morphology still remained even after calcined at higher temperature, except an increase in diameter and decrease in length in comparison with the β-MnO_2 nanorods. Fig.3c shows the XRD pattern of $LiMn_2O_4$ nanorods. The observed XRD pattern of the $LiMn_2O_4$ is in good agreement with the standard pattern of the $LiMn_2O_4$ (JCPDS card No. 88-1026) and confirmed the formation of cubic spinel phase with *Fd*3*m* space group. There is no β-MnO_2 peaks observed in the pattern indicates that the reaction between β-MnO_2 and $LiOH.H_2O$ at 700 ^oC produced high pure crystalline $LiMn_2O_4$ phase.

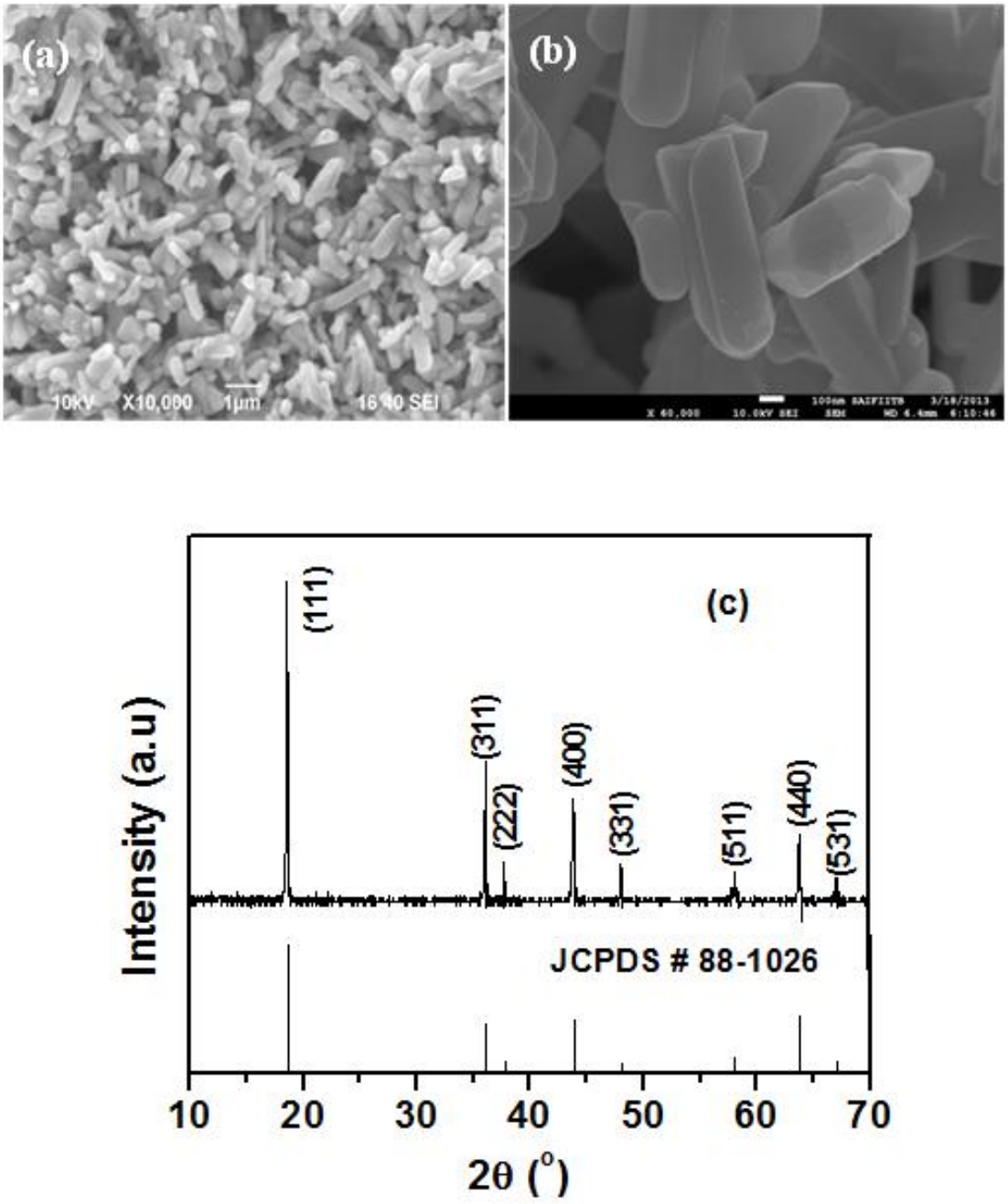

Figure 3. FE-SEM images (a,b) and XRD pattern(c) of $LiMn_2O_4$ nanorods, obtained at 700^oC for 10 h.

Fig.4 (a & b) shows the typical FTIR spectra of β-MnO_2 (Reaction time: 90 min) and $LiMn_2O_4$ nanorods. From fig.4a, the FTIR bands observed at 726 cm^{-1}, 539 cm^{-1} and 422 cm^{-1} are assigned to the Mn-O vibrations of the rutile type MnO_6 octahedra framework, which confirmed the formation of β-MnO_2 structure [26]. As shown in fig.4b, the spinel $LiMn_2O_4$ sample exhibited two peaks at 612 cm^{-1} and 510 cm^{-1} are attributed to the O-Mn-O vibrations in $LiMn_2O_4$ structure [27]. Raman spectrum of spinel $LiMn_2O_4$ nanorods is shown in fig.4c. From fig.4c, the Raman peak observed at 640 cm^{-1} corresponds to the symmetric Mn-O stretching vibration of MnO_6 octahedra and it is attributed to the A_{1g} mode in the O_h^7 symmetry.

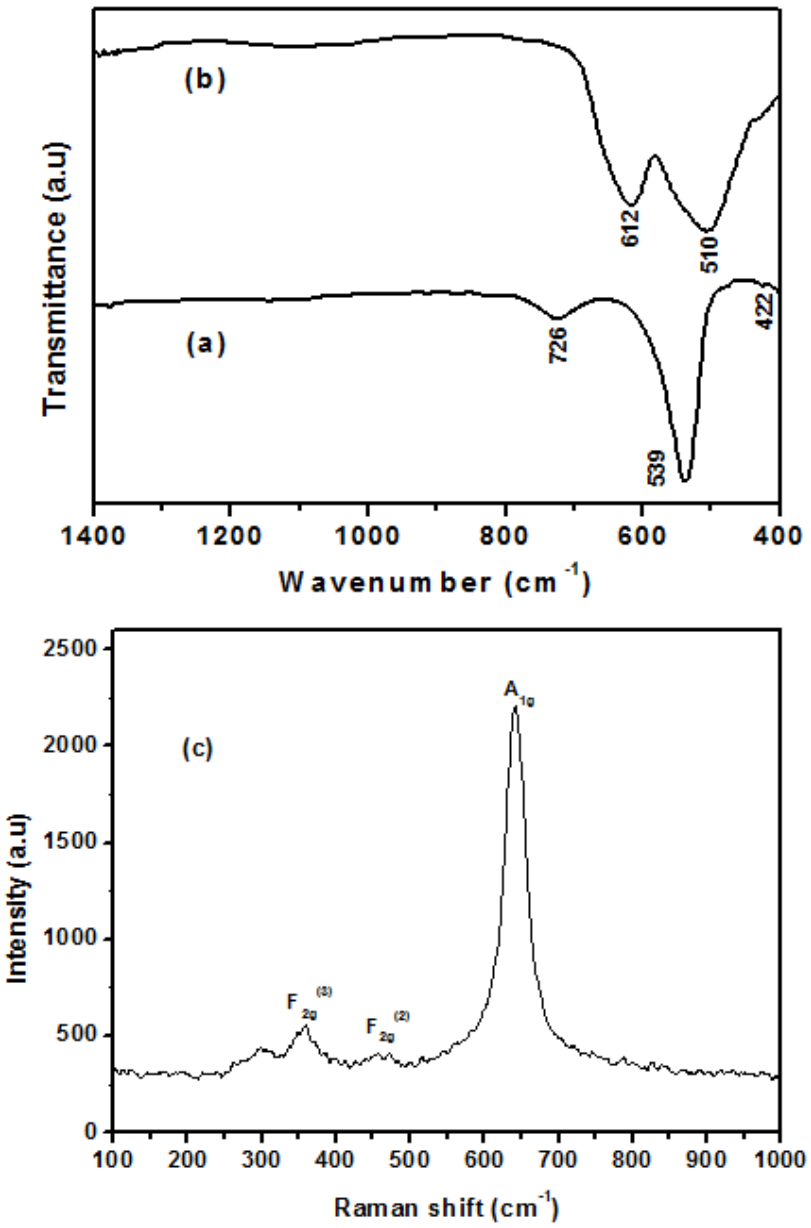

Figure 4. FTIR spectra of as-obtained a) β-MnO_2 (Reaction time: 90 minutes) and b) $LiMn_2O_4$ nanorods. c) Raman spectrum of spinel $LiMn_2O_4$ nanorods.

The manganese ions in the spinel $LiMn_2O_4$ exhibit a charge disproportionation as $LiMn^{3+}Mn^{4+}O_4$, which results in the formation of isotropic $Mn^{4+}O_6$ octahedra and locally distorted $Mn^{3+}O_6$ octahedra. Thus, the observed broadness of A_{1g} mode is due to stretching vibrations of both MnO_6^{9-} and MnO_6^{8-} octahedra in spinel $LiMn_2O_4$ [28, 29]. The observed peaks at 464 cm^{-1} and 357 cm^{-1} are attributed to the $F_{2g}^{(2)}$ and $F_{2g}^{(3)}$ modes, respectively. The $F_{2g}^{(3)}$ mode corresponds to the Li-O vibration, which has a connection to the tetrahedral cation movements [28,30]. The low intensity band observed at 300 cm^{-1} might be related to the cationic disorder in the material.

The TEM images and SAED pattern (Figs.5a, b, c and d) further revealed that the $LiMn_2O_4$ obtained at 700 ^oC exhibits the high-quality cubic spinel $LiMn_2O_4$ nanorods. The nanorods were well-dispersed and maintained one-dimensional (an average diameter of 190 nm) morphology. The corresponding selected area of the electron diffraction (SAED) pattern (Fig.5d) supports the formation of high-quality cubic spinel structure of $LiMn_2O_4$ nanorods.

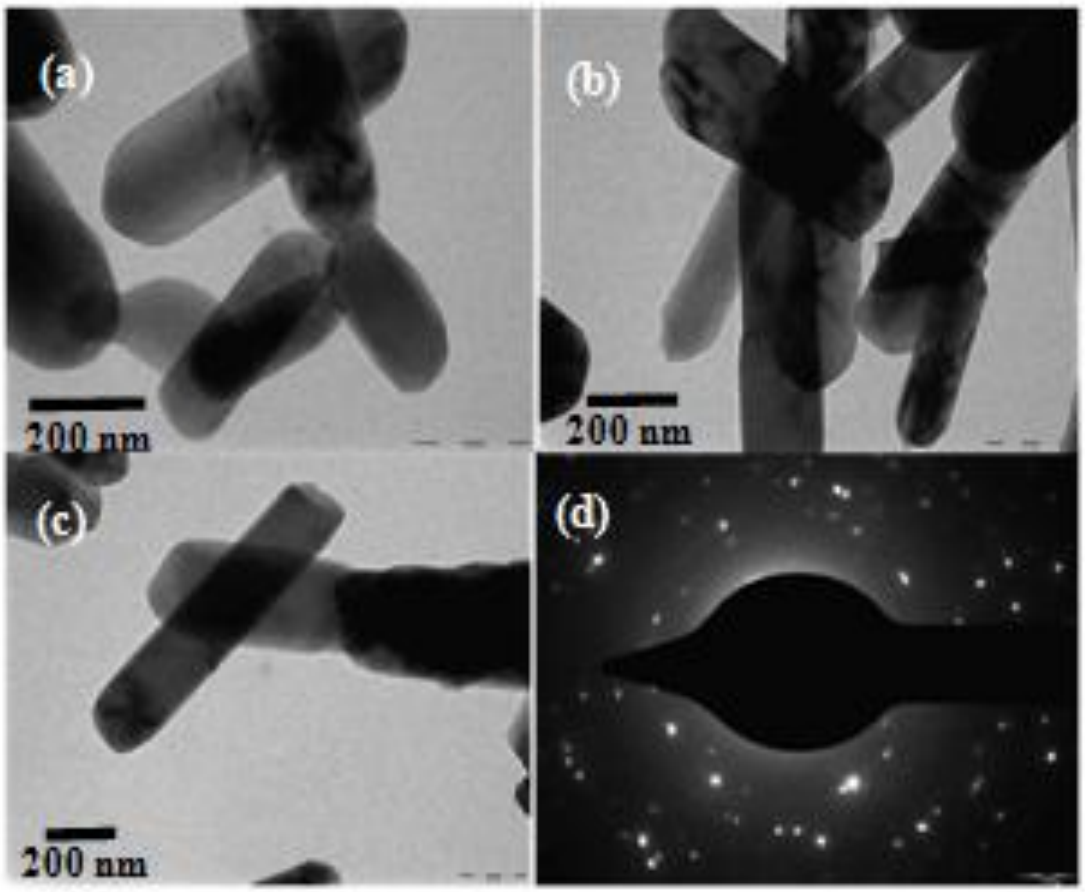

Figure 5. TEM images (a, b, c) and SAED (d) pattern of the $LiMn_2O_4$ nanorods.

Fig.6 shows the cyclic voltammetry (CV) curve of the spinel $LiMn_2O_4$ nanorods for the 1st cycle at a scan rate of 0.2 mVs^{-1}, at room temperature. Fig.6 shows two oxidation peaks at potentials of 4.1 and 4.3 V represent the typical two stage de-intercalation of lithium ions from spinel $LiMn_2O_4$ structure. During the cathodic scan, the reduction peaks appear at 3.8 and 3.95 V. The main anodic and cathodic peaks difference is 200 mV, which indicates the high reversibility of the system.

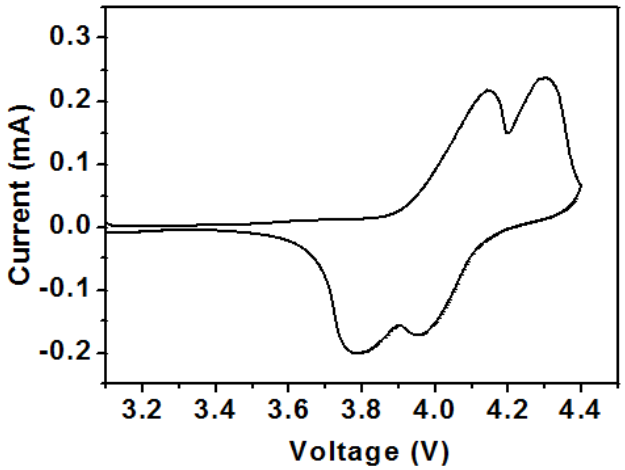

Figure 6. CV curve of the spinel $LiMn_2O_4$ nanorods at 1st cycle with a scan rate of 0.2 mVs^{-1}.

The Nyquist plots of the spinel $LiMn_2O_4$ electrode at the first cycle charging profile are shown in fig.7a. The observed impedance spectra show a potential independent semicircle in high frequency region, a potential dependent semicircle in the middle frequency region and a Warburg element and steep line in lower frequency region.

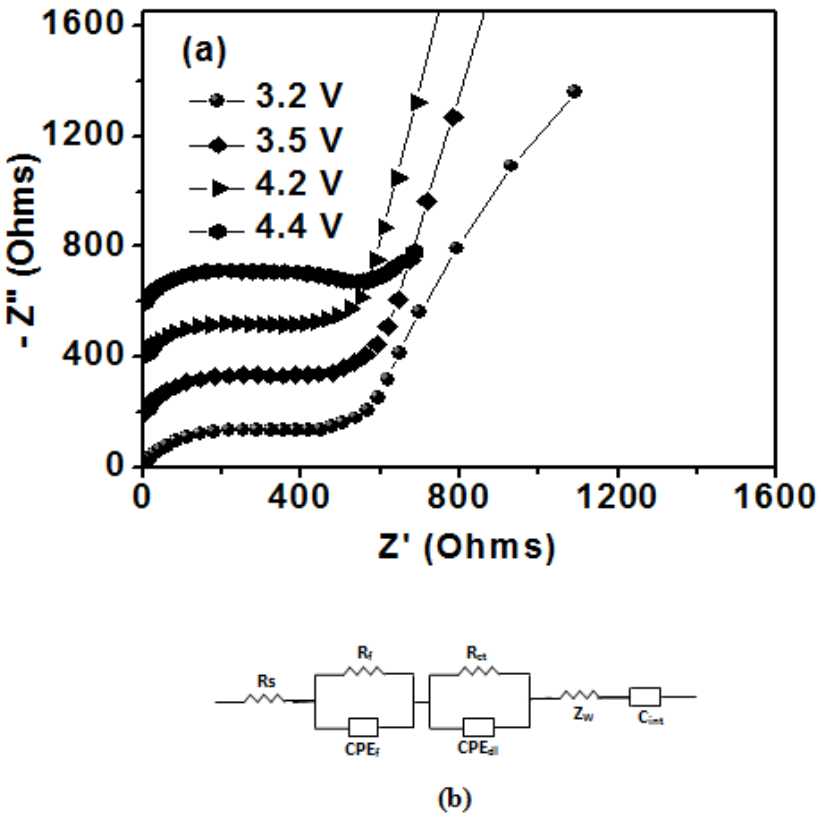

Figure 7. (a) Nyquist plots of the spinel $LiMn_2O_4$ nanorods electrode at different potentials during the 1st cycle charging process and (b) Equivalent circuit.

The EIS data is often interpreted by presenting the electrical equivalent circuit as shown in fig.7b. From fig.7b, the equivalent circuit describes two constant phase elements associated with the charge transfer process and passivation of the film. The Warburg part (Z_w) is associated with the diffusion of lithium ions in the solid matrix, R_s represents the electrolyte resistance, R_p and R_{ct} are the resistances of the passivation film (SEI) and the charge transfer reaction, respectively. The semicircle in the high frequency region is related to the migration of Li^+ through the surface film of $Li_xMn_2O_4$. The middle frequency semicircle is related to the charge transfer (R_{ct}) at electrode-electrolyte interface. The Warburg type element and steep line at lower frequencies reflect the diffusion and occupation of Li^+ ions in the inserted sites, respectively. Fig.7a, shows the decrease of charge-transfer resistance (R_{ct}) with potential. At higher potentials, the Li^+ diffusion and Li^+ occupation take place simultaneously and facilitate Li^+ insertion into the lattice, which results in the decrease of charge-transfer resistance (R_{ct}) [31].

The charge–discharge curves of the spinel $LiMn_2O_4$ nanorods studied at 0.1 C-rate in the potential range 3.1V - 4.4 V are shown in fig 8. Both the charge and discharge curves exhibited two pseudoplateaus at 3.9V and 4.1V, indicate the typical two-stage lithium de-intercalation and intercalation behavior of the cubic spinel $LiMn_2O_4$ structure. The charge and discharge capacities were obtained respectively are 146 & 132 $mAhg^{-1}$ at the first cycle and 98 & 96 $mAhg^{-1}$ at the 50^{th} cycle. However, the first cycle irreversible capacity is high and decreases with cycling. The complete charge and discharge capacities vs number of cycles and their corresponding columbic efficiency are shown in fig.9.

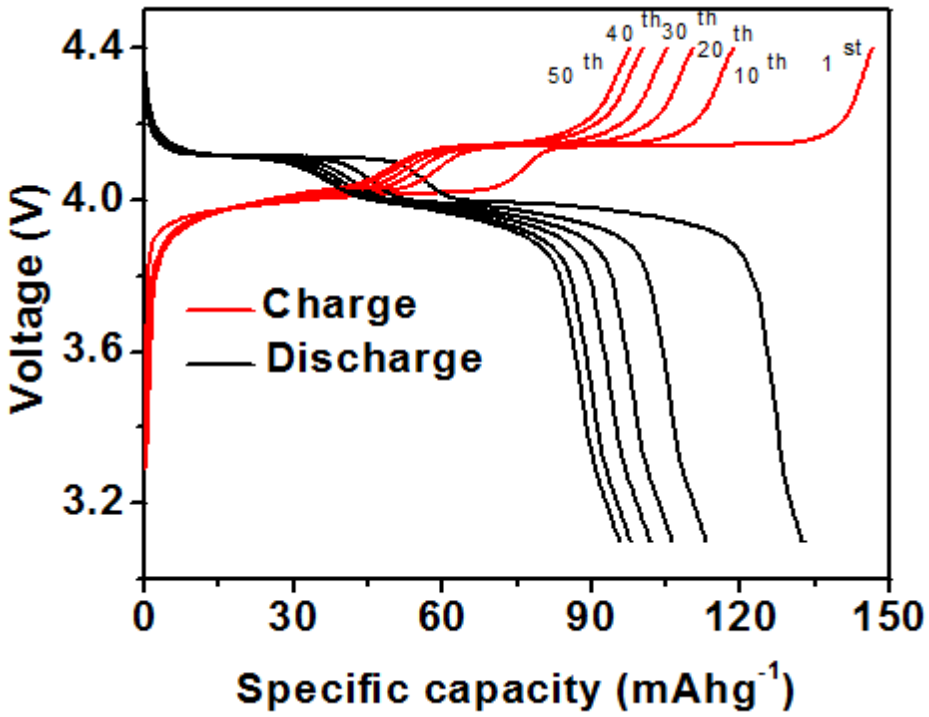

Figure 8. The charge-discharge curves of the spinel $LiMn_2O_4$ nanorods (at 0.1 C and voltage ranges: 3.1V - 4.4 V).

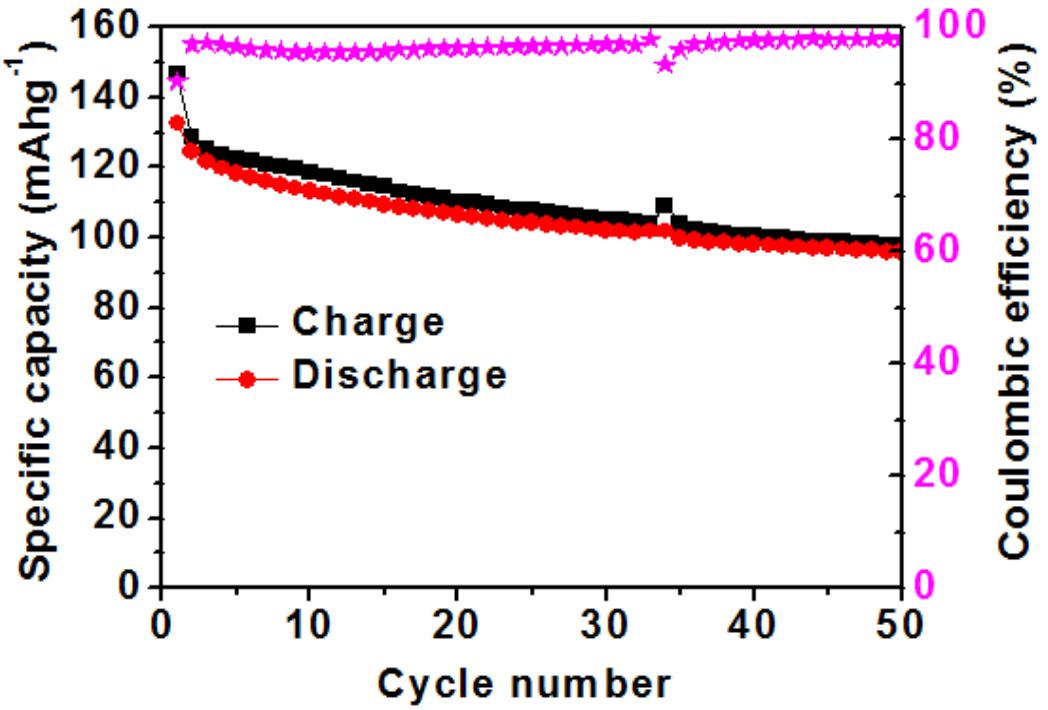

Figure 9. Specific capacity and coulombic efficiency as function of cycle numbers of the spinel $LiMn_2O_4$ nanorods (0.1 C and voltage ranges: 3.1V - 4.4 V).

Further to investigate the rate capability of the $LiMn_2O_4$ nanorods, the electrochemical tests were performed at higher C-rates (1C, 2C, 5C & 10 C). The discharge capacities as function of number of cycles at different C-rates are presented in fig.10. The discharge capacities obtained are 75 $mAhg^{-1}$, 65 $mAhg^{-1}$, 48 $mAhg^{-1}$ and 34 $mAhg^{-1}$, respectively at 1C, 2C, 5C and 10C.

It is observed that the discharge capacities decrease with increase of C-rate. The observed capacity with different C-rate was discussed based on the electrode kinetics. At lower rates, the intercalation/de-intercalation of Li^+ ions in and out of the one-dimensional nanorods is favorable and hence, leading to higher capacity. At higher rates, the intercalation/de-intercalation of Li^+ ions undergoes only at the surface of the electrode particle, and hence the capacity is lower. It is well understood that the one-dimensional nanorod materials are stable even at higher C-rates without any distraction of the electrode structure. The identification of the materials characteristic such as particle morphology retention of the electrode at different C-rates is important for understanding the stability of the structure and electrochemical performance as well. The capacity test of the lithium-ion cells were carried out at 1C, 2C, 5C, 10C and followed by 1C. By comparing the capacities of the lithium-ion cell at 1C (fig.10) shows that the capacity of the cell (after 10C test) is found to be marginally improved, which indicates better reversibility of the spinel $LiMn_2O_4$ nanorods.

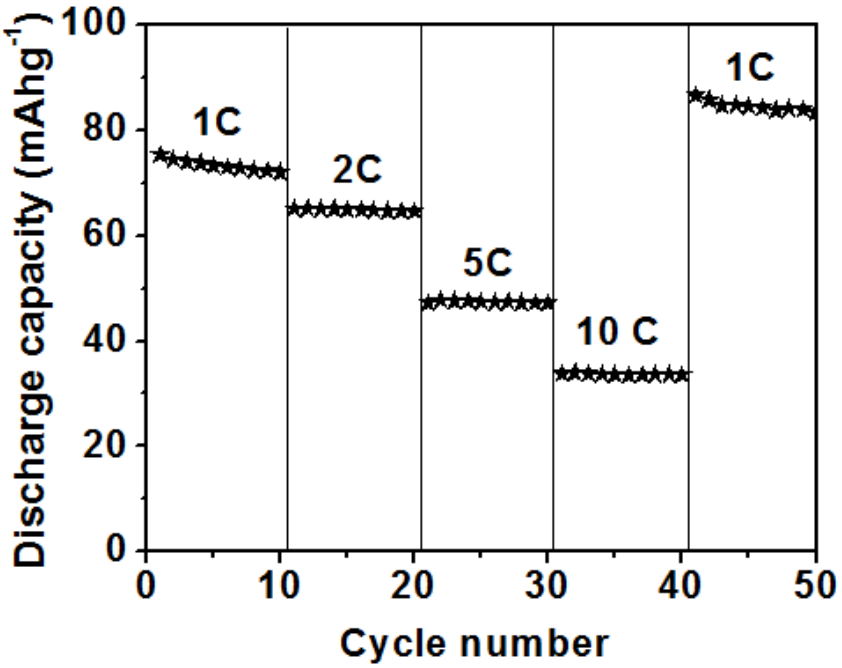

Figure 10. Discharge capacity versus number of cycles of $LiMn_2O_4$ nanorod cathode at different C rates (1C, 2C, 5C &10C).

The charge and discharge curves of $LiMn_2O_4$ nanorods electrode at different C-rates are shown in fig.11. From fig.11, it is observed that the pseudoplateau of discharge curve moves downward with increase of C-rate. At lower C-rates, the cell operates closer to the equilibrium condition, whereas at higher C-rates, the operating voltage decreases due to low conductive organic electrolyte [32].

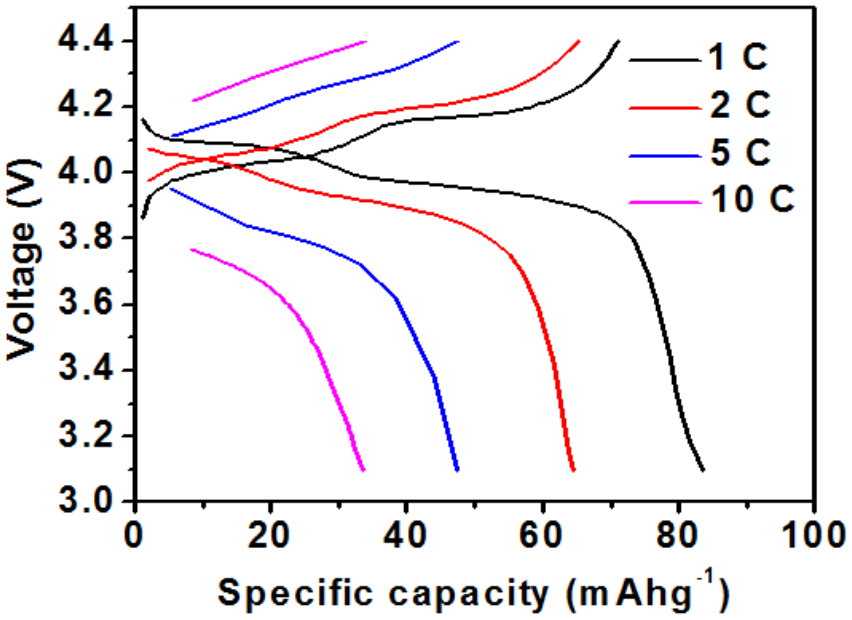

Figure 11. Charge and discharge profiles of spinel $LiMn_2O_4$ nanorods, obtained at 1C, 2C, 5C &10C.

As-obtained spinel $LiMn_2O_4$ nanorods are showing good cycleability with better coulombic efficiency due to their one-dimensional morphology and phase pure crystallinity. These data indicate that the large surface-to-volume ratio of the nanorods enhances the kinetics of the spinel $LiMn_2O_4$.

4. CONCLUSIONS

The microwave assisted hydrothermal synthesis is found to be a powerful method for the preparation of β-MnO_2 nanorods. The prepared β-MnO_2 nanorods were effectively converted into cubic spinel $LiMn_2O_4$ nanorods by a simple solid state reaction. The spinel $LiMn_2O_4$ nanorods are capable of delivering a stable discharge capacity over 50 cycles, with good capacity retention and coulombic efficiency. The nanorod morphology with high single-crystallinity appears to improve the kinetic properties of the electrode material through a large surface area to volume ratio. The facile microwave synthesis is extensively applicable and provides an opportunity for industry to design and develop novel nanostructured electrode materials for advanced lithium-ion batteries.

ACKNOWLEDGEMENT
NS is grateful to UGC, Govt. of India for providing financial support in the form of research project [No.:39-460/2010(SR)]. BNR is thankful to DST, Govt. of India for awarding the INSPIRE fellowship (No.:DST/INSPIRE Fellowship/2011/241) for pursuing Doctoral degree. PM & NS are grateful to BRFST, Govt. of India for providing financial support in the form of research project (BRFST/NFP/2012/FEB/N/10). MV is grateful to the management of amararaja for their support.

References

1. M. Armand and J.M.Tarascon, *Nature*, 451(2008) 652
2. H. Nishide and K. Oyaizu, *Science*, 319 (2008) 737
3. B. Scrosati, *Nature*, 373 (1995) 557
4. S.Y. Chung, J.T. Bloking and Y.M. Chiang, *Nat. Mater*, 1 (2002) 123
5. Z. Yang, Q. Qiao and W. Yang, *Electrochim. Acta*, 56 (2011) 4791
6. G.G. Amatucci, J.M.Tarascon and L.C. Klein, *Solid State Ionics*, 83 (1996) 167
7. M.M.Thackeray, P.J. Johnson, L.A. Depicciotto, P.G. Bruce and J.B. Goodenough, *Mater. Res. Bul*, 19 (1984) 179
8. M.M. Thackeray and A.J. Dekock, *Solid state chem*, 74 (1988) 414
9. M.Jayalakshmi, M. Mohan Rao and F.Scholz, *Langmuir*, 19 (2003) 8403
10. J. Cabana, T. Valde´s-Solı´s, M.R. Palacı´n, J. Oro´-Sole´, A. Fuertes,G. Marba`n and A.B. Fuertes, *J. Power Sources*, 166 (2007) 492
11. J.Y.Luo, Y.G. Wang, H.M. Xiong and Y.Y. Xia, *Chem. Mater*, 19 (2007) 4791
12. A. Blyr, C. Sigala, G.G. Amatucci, D. Guyomard, Y. Chabre and J.M. Tarascon, *J. Electrochem. Soc*, 145 (1998) 194
13. D.K. Kim, P. Muralidharan, H.W. Lee, R. Ruffo, Y. Yang, C.K. Chan, H. Peng, R.A. Huggins and Y. Cui, *Nano Lett*, 8(11) (2008) 3948
14. N. Li, C.J. Patrissi, G.L. Che and C.R. Martin, *J.Electrochem. Soc*, 147(6) (2000) 2044
15. M.Nishizawa, K. Mukai, S. Kuwabata, C.R.Martin and H. Yama, *J. Electrochem. Soc*, 144 (1997) 1923
16. C.J.Curtis, J.X. Wang and D.L. Schulz, *J. Electrochem. Soc*, 151(4) (2004) 590

17. K. Du and H. Zhang, *J. Alloys Compd*, 352 (2003) 250
18. D. Kovacheva, H. Gadjov, K. Petrov, S. Mandal, M.G. Lazarraga, L. Pascual, J.M. Amarilla, R.M. Rojas, P. Herrero and J.M. Rojo, *J.Mater. Chem*, 12 (2002) 1184
19. S. Nieto, S.B. Majumder and R.S. Katiyar, *J. Power Sources*, 136 (2004) 88
20. C.Ze-hua, H. Ke-long,L. Su-qin and W. Hai-yan, *Trans. Nonferrous Met.Soc. China*, 20 (2010) 2309
21. D. Zhan, Q. Zhang, X. Hu, G. Zhu and T. Peng, *Solid State Ionics*, 239 (2013) 8
22. W. Tang, L.L. Liu, S. Tian, L. Li, L.L. Li, Y.B. Yue, Y. Bai, Y.P. Wu, K. Zhu and R. Holze, *Electrochem. Commun*, 13 (2011) 1159
23. I.Bilecka, I. Djerdj and M. Niederberger, *Chem. Commun*, (2008) 886
24. J.A. Gerbec, D. Magana, A. Washington and G.F. Strouse, *J. Am.Chem. Soc*, 127(45) (2005) 15791
25. A.B. Panda, G. Glaspell and M.S.M. El-Shall, *J. Am. Chem. Soc*, 128 (2006) 2790
26. R.M. Potter and G.R. Rossman, *Am. Mineral*, 64 (1979) 1199
27. A. Rougier, K.A. Striebel, S.J. Wen, T.J. Richardson, R.P. Reade and E. Cairns, *J. Appl. Surf. Sci*, 134 (1998) 107
28. C.M. Julien and M. Massot, *J. Phys.: Condens. Matter*, 15 (2003) 3151
29. C.V. Ramana, M. Massot and C.M. Julien, *Surf. Interface Anal*., 37 (2005) 412
30. C. Julien, M. Massot, S. Rangan, M. Lemal and D. Guyomard, *J. Raman Spectrosc*, 33 (2002) 223
31. D. Lu, W. Li, X. Zuo, Z. Yuan and Q. Huang, *J. Phys.Chem. C*, 111 (2007) 12067
32. D. Linden and T.D. Reddy, *in Handbook of Batteries, 3rd ed*., McGraw-Hill, New York (2002)